Electronic Supplementary Material

Engineering highly-exposed nickel nanoparticles within a nitrogen-doped carbon matrix for efficient CO_2 electroreduction to CO

Can Yang[1], Bingyuan Dai[1], Minxuan Wang[1], Hui Xu[1], Hongbing Zheng[1], Cheng Ma[2], Licheng Ling[3], Jitong Wang (✉)[1,4]

1 State Key Laboratory of Green Chemical Engineering and Industrial Catalysis, School of Chemical Engineering, East China University of Science and Technology, Shanghai 200237, China

2 Key Laboratory of Specially Functional Polymeric Materials and Related Technology (Ministry of Education), School of Materials Science and Engineering, East China University of Science and Technology, Shanghai 200237, China

3 Key Laboratory of Specially Functional Polymeric Materials and Related Technology (Ministry of Education), School of Chemical Engineering, East China University of Science and Technology, Shanghai 200237, China

4 University Engineering Research Center of Green Chemical New Materials, School of Chemistry and Chemical Engineering, Guangxi University, Nanning, Guangxi 530004, China.

E-mail: wangjt@ecust.edu.cn

Synthesis of Ni$_{SA}$-BCN@C

The preparation of Ni$_{SA}$-BCN@C was the same procedure as that for Ni$_{NP}$-BCN@C, except that the volume of $NiCl_2 \cdot 6H_2O$ solution (2 mg ml^{-1}) was adjusted to 500 μl.

Synthesis of BCN@Ni$_{NP}$/C

A 1 g sample of BCN@C was thoroughly mixed with 3.25 mL of a 2 mg·mL^{-1} $NiCl_2 \cdot 6H_2O$ solution in a mortar and dried completely. The resulting material was transferred to a tube furnace and heated from ambient temperature to 550 °C at a rate of 1°C·min^{-1} under a nitrogen atmosphere, maintaining this temperature for 2 h. The temperature was then increased to 800 °C at the same rate and held for an additional 2 h. After cooling to ambient temperature under natural conditions, the sample was subjected to acid washing in an HCl solution for 12 h to yield the BCN@Ni$_{NP}$/C catalyst.

Electrochemical Measurement Details

Gaseous products at the cathode were analyzed using an online gas chromatograph over 2400 s, with voltage changes every 15 min. Carbon-based compounds were detected via a flame ionization detector (FID), and hydrogen was quantified using a thermal conductivity detector (TCD), with data collected every 12 min to determine product composition. Liquid products were analyzed via proton nuclear magnetic resonance (NMR) spectroscopy using a Bruker Avance III HD 400 MHz spectrometer in deuterated DMSO.

Linear sweep voltammetry (LSV) was performed to compare the catalyst responses in CO_2- and Ar-saturated 0.5 M $KHCO_3$ electrolytes, with reaction energy barriers assessed by comparing LSV curve onset potentials for CO_2RR and HER. Cyclic voltammetry (CV) was conducted from open circuit potential (OCP) between +0.05 V and −0.05 V vs. RHE, with six cycles per potential sweep. The double-layer capacitance of the catalyst can be determined from the CV scan curve, thereby estimating the size of the electrochemically active surface area. Electrochemical impedance spectroscopy (EIS) was performed at OCP with a frequency range of 100 kHz to 0.1 Hz and a 5 mV rms AC amplitude.

In situ Fourier Transform Infrared monitoring of the catalytic reaction process was performed using a Thermo Scientific Nicolet iS50 spectroscopy system. The reaction cell consists of a polytetrafluoroethylene base, a glass reactor, and a three-electrode system. Catalyst ink was evenly coated onto a gold-coated single-crystal silicon pillar. A background spectrum was collected at an initial potential, followed by infrared spectra at different reaction potentials. Analysis of the resulting infrared spectra revealed intermediate products of the catalytic reaction, thereby revealing the progress of the catalytic reaction.

Computational Details

Spin-polarized density functional theory (DFT) calculations were performed using the projector-augmented wave (PAW)[1] method, implemented in the Vienna Ab-initio Simulation Package (VASP) code[2, 3]. Electron exchange correlation was expressed by the Perdew-Burke-Ernzerhof (PBE) functional within the generalized gradient approximation (GGA)[4]. Plane-wave cut-off energies of 600 eV and 400 eV were used for the optimization of bulk and slab structures, respectively. The slab models were constructed using a 3 × 3 supercell containing five atomic layers. A vacuum layer of 20 Å thickness was added to all slab structures to prevent interactions between periodic replicas in the simulations. The cut-off energy for the plane-wave basis was set to 500 eV. The convergence criteria were set to 10^{-5} eV in total energy and 0.05 eV $Å^{-1}$ in force. The Gibbs free energy (ΔG) was calculated using the following equation:

$$\Delta G = \Delta E_{DFT} + \Delta E_{ZPE} - T\Delta S \tag{S1}$$

where ΔE_{DFT}, ΔE_{ZPE}, and ΔS are the energy change, zero-point energy correction, and reaction entropy change respectively.

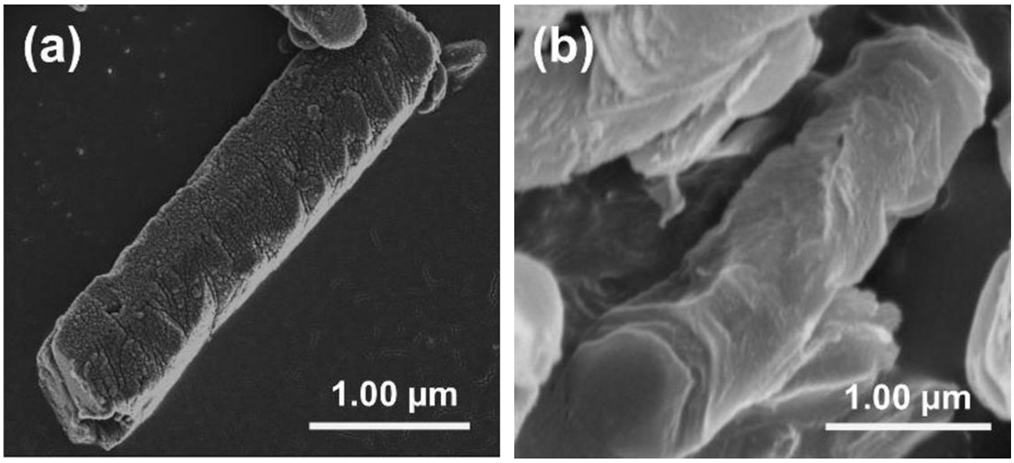

Figure S1. SEM image of BCN@C (a) before and (b) after carbonized. Before carbonized, a uniform, fuzzy surface and a regular rod-like structure confirming successful glucose coating on the g-C_3N_4 precursor. Carbonized BCN@C material has a significantly reduced thickness and increased surface wrinkling.

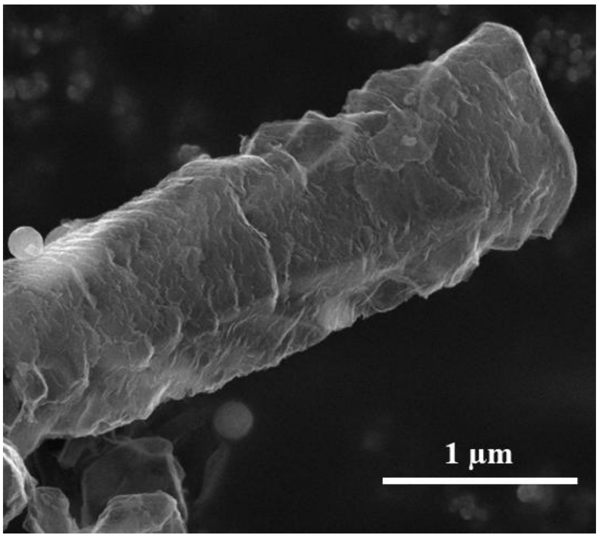

Figure S2. SEM image of $\mathrm{Ni_{SA}}$-BCN@C. It retains a rod-like structure similar to BCN@C.

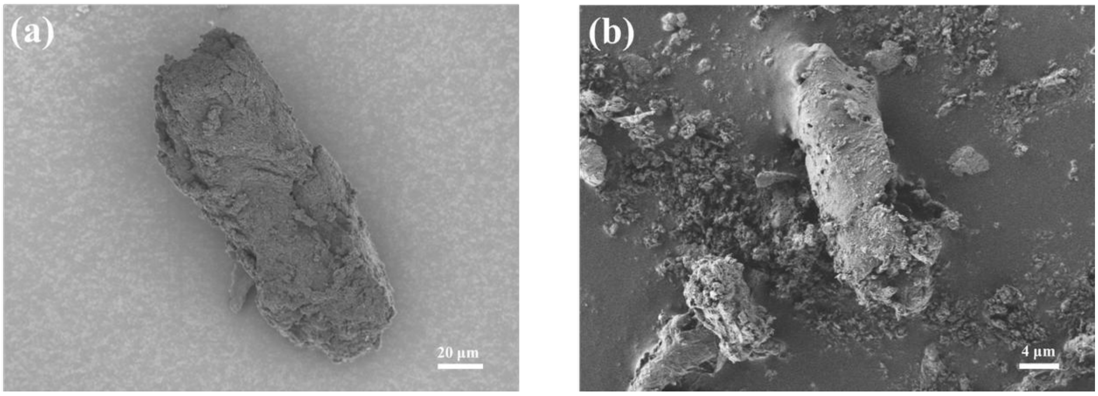

Figure S3. SEM image of BCN@$\mathrm{Ni_{NP}}$/C (a) before and (b) after carbonized. High-temperature-induced Ni NPs aggregation leads to an increase in the size of the rod-like structure.

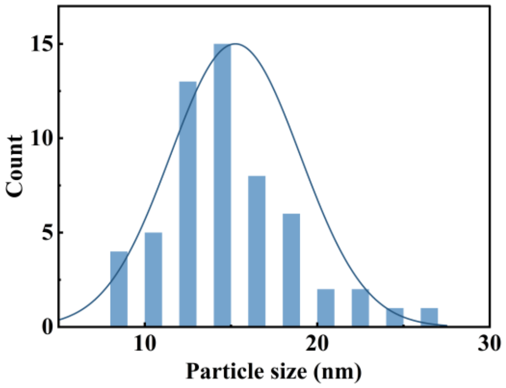

Figure S4. The particle size distribution map of $\mathrm{Ni_{NP}}$-BCN@C. The most of nickel nanoparticles have a diameter of approximately 15 nm.

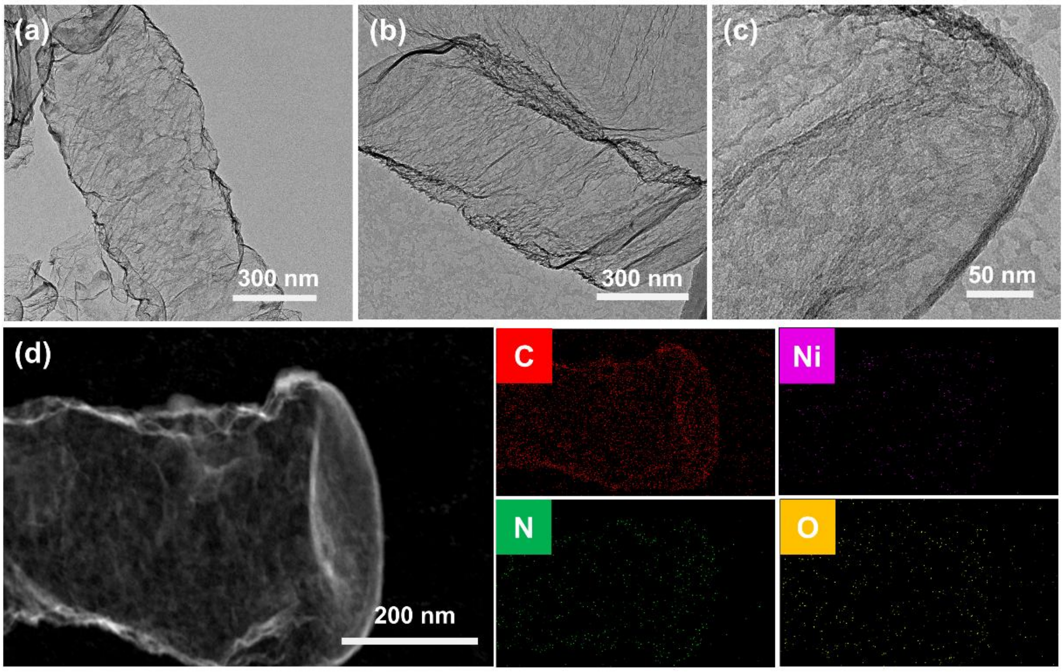

Figure S5. (a) and (c) TEM image of catalyst Ni$_{SA}$-BCN@C. (b) TEM images of catalyst BCN@C. (d) Dark-field TEM image of catalyst Ni$_{SA}$-BCN@C and EDS scan image of surface elements. The catalysts Ni$_{SA}$-BCN@C and BCN@C exhibit a prominent hollow structure, similar to Ni$_{NP}$-BCN@C, no discernible pore structure in Ni$_{SA}$-BCN@C. Elemental mapping of Ni$_{SA}$-BCN@C shows uniform dispersion of C, N, O, and Ni, with Ni SAs without nanoparticle formation.

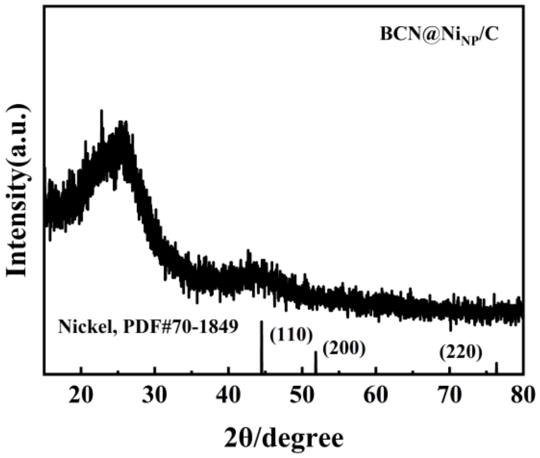

Figure S6. XRD image of BCN@Ni$_{NP}$/C. BCN@Ni$_{NP}$/C displays sharp peaks at 2θ = 44.5°, 51.8°, and 76.4°, corresponding to metallic Ni (PDF card).

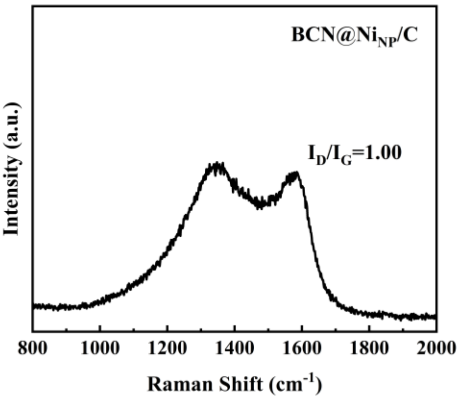

Figure S7. Raman pattern of BCN@Ni$_{NP}$/C, with an intermediate I_D/I_G ratio of 1.00.

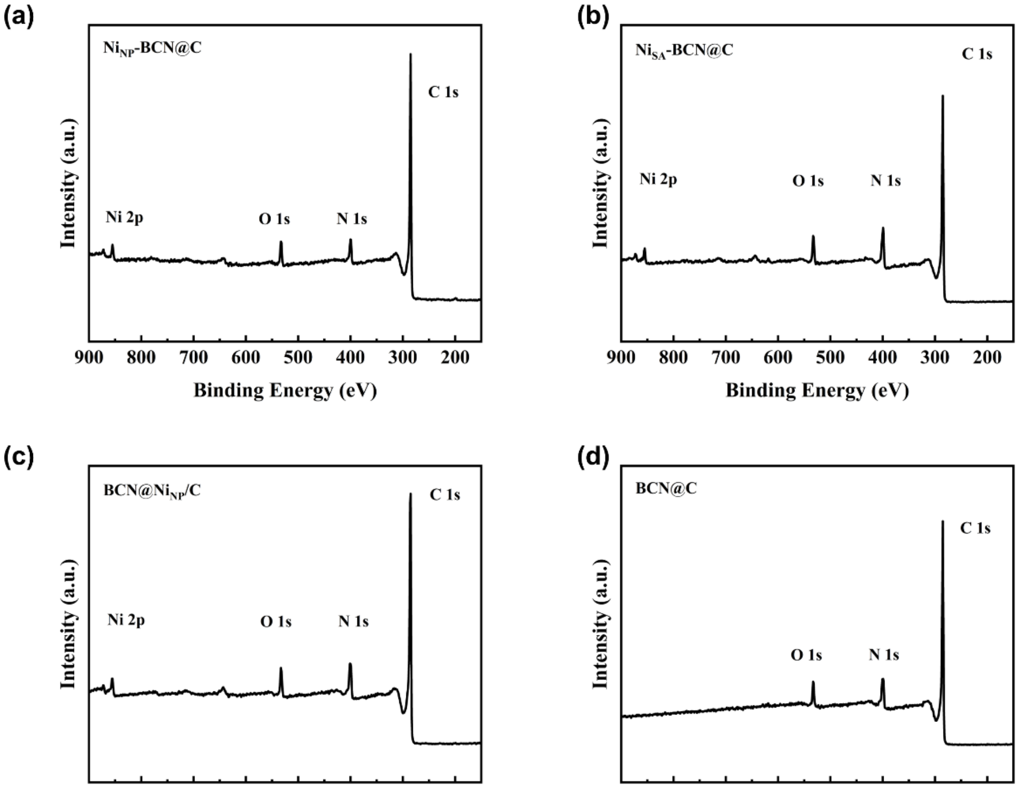

Figure S8. The full spectra of XPS for (a) Ni$_{NP}$-BCN@C, (b) Ni$_{SA}$-BCN@C, (c) BCN@Ni$_{NP}$/C and (d) BCN@C. All four catalysts exhibit O 1s, N 1s, and C 1s peaks, confirming the presence of C, N, and O as the core framework elements.

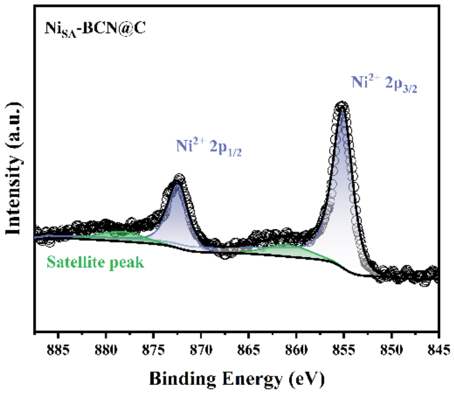

Figure S9. Ni 2p fine spectra of XPS for NiSA-BCN@C. Ni species exist in the oxidation state of Ni^{2+}, Ni^0 is not detected.

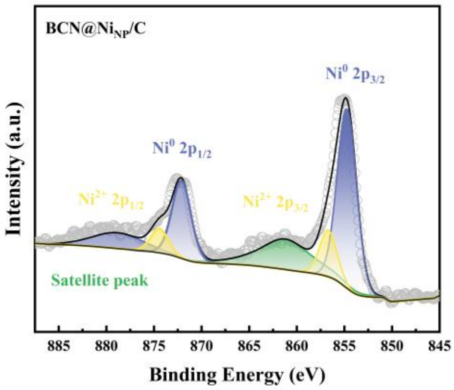

Figure S10. Ni 2p fine spectra of XPS for BCN@NiNP/C, showing the $2p^{3/2}$ and $2p^{1/2}$ peaks of Ni^0, indicating the presence of Ni NPs.

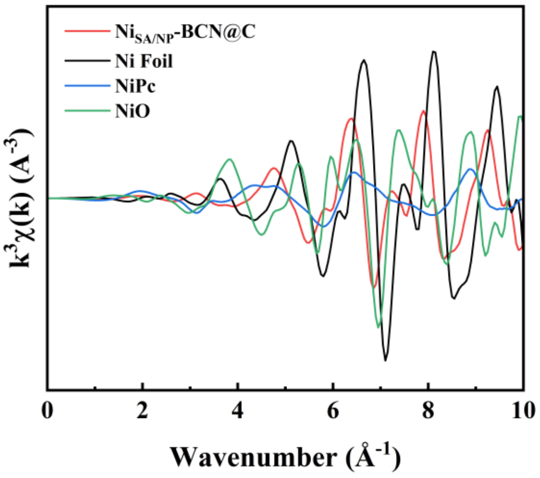

Figure S11. K-edge EXAFS spectrum of Ni in K-space of NiNP-BCN@C. The figure shows a peak between Ni-N and Ni-Ni bonds, revealing that Ni is mainly metallic

with minor N coordination.

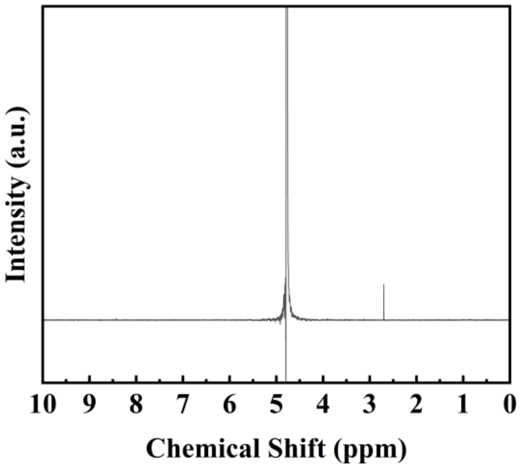

Figure S12. ^{1}H NMR spectrum after electrochemical test. This proves that no liquid-phase products were formed.

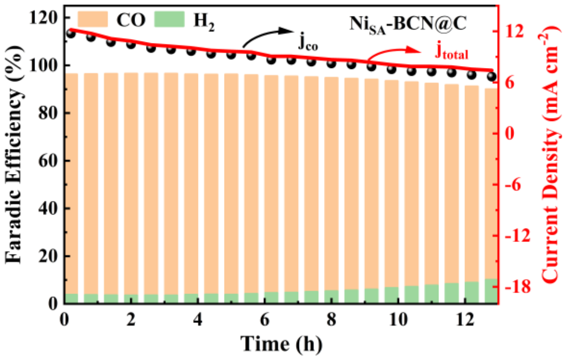

Figure S13. Stability test of Ni$_{SA}$-BCN@C in H-cell. The FE of Ni$_{SA}$-BCN@C dropped to 90% after 12 h, with current density decreasing from 12 mA cm^{-2} to 7.4 mA cm^{-2}.

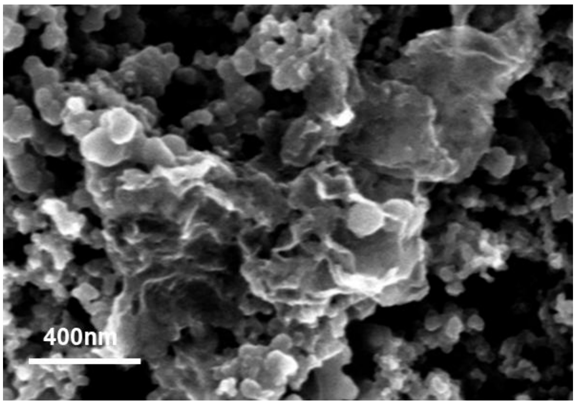

Figure S14. SEM image after 32 h stability test of Ni$_{NP}$-BCN@C in H-cell. The

hollow carbon layer breaks down under prolonged electroreduction, and the aggregation of Ni nanoparticles leads to hydrogen evolution.

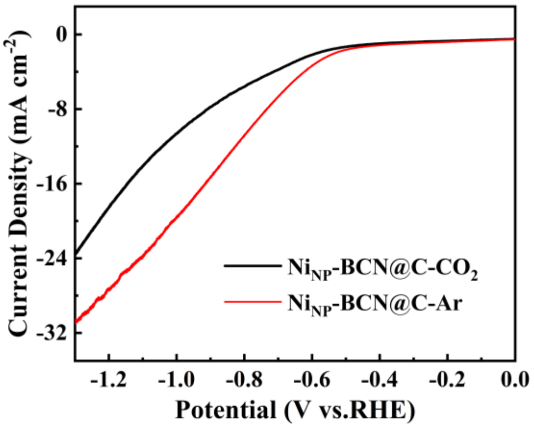

Figure S15. LSV scanning curves of Ni$_{NP}$-BCN@C in different atmosphere, confirming Ni$_{NP}$-BCN@C has activity for the CO$_2$RR.

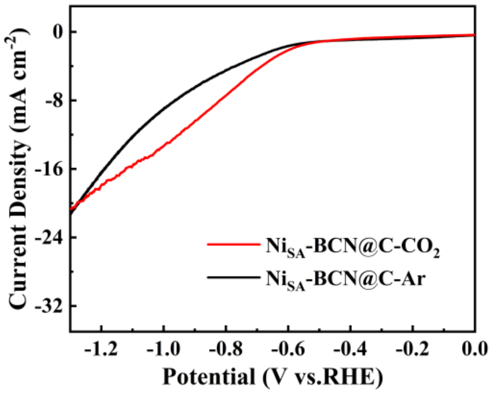

Figure S16. LSV scanning curves of Ni$_{SA}$-BCN@C in different atmosphere. The current density in Ar approaches that in CO$_2$ at higher potentials, with the CO$_2$ curve showing a declining trend, suggesting reduced activity.

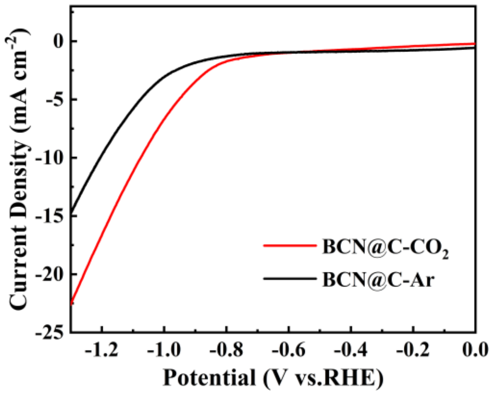

Figure S17. LSV scanning curves of BCN@C in different atmospheres.

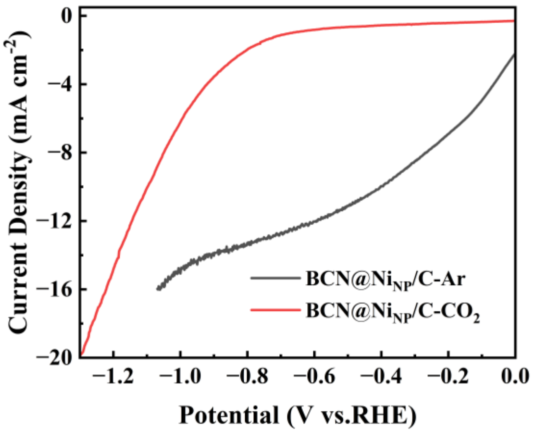

Figure S18. LSV scanning curves of BCN@Ni$_{NP}$/C in different atmospheres.

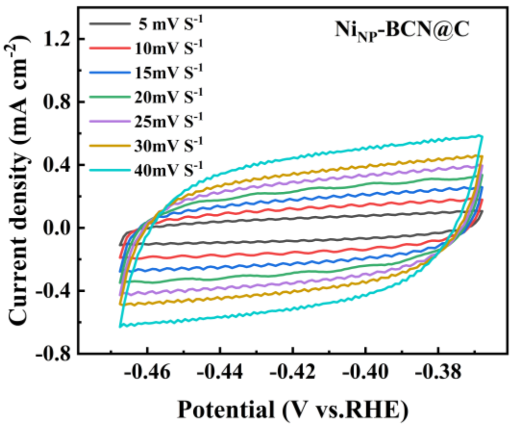

Figure S19. CV scan curve of Ni$_{NP}$-BCN@C.

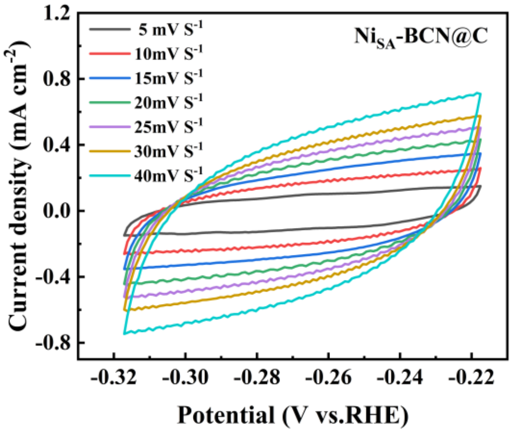

Figure S20. CV scan curve of Ni$_{SA}$-BCN@C.

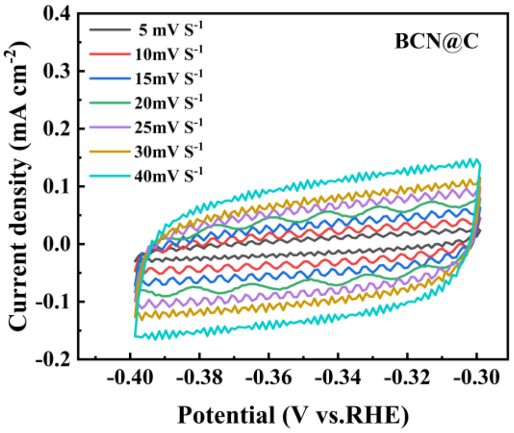

Figure S21. CV scan curve of BCN@C.

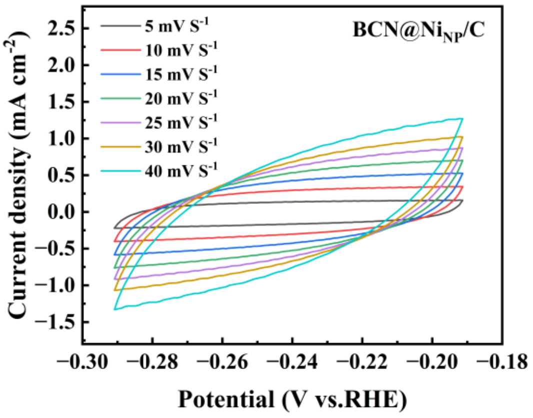

Figure S22. CV scan curve of BCN@Ni$_{NP}$/C.

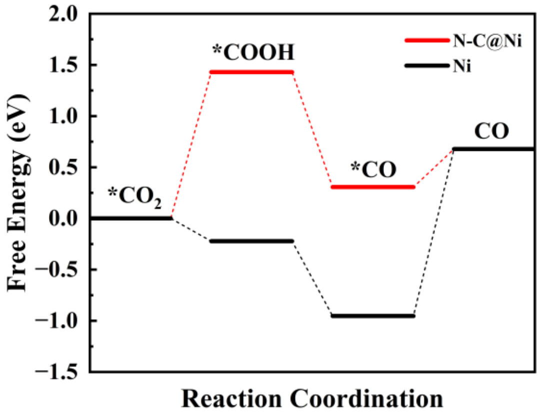

Figure S23. Free energy change of the reaction pathway over N-C@Ni and bare Ni.

Table S1 E_0 and structure parameters from the EXAFS fitting of Ni K-edge.

Scattering pair	**s0^2**	**CN**	**R(Å)**	**σ^2(Å)**	**R factor**	**E_0(eV)**
Ni-Ni	0.50	12	2.48	0.006	0.001	8345.25

Reference

1. Blöchl PE. Projector augmented-wave method. Physical Review B, 1994. **50**(24): 17953–17979.
2. Kresse G, J Furthmüller. Efficiency of ab-initio total energy calculations for metals and semiconductors using a plane-wave basis set. Computational Materials Science, 1996. **6**(1): 15–50.
3. Kresse G, J Furthmüller. Efficient iterative schemes for ab initio total-energy calculations using a plane-wave basis set. Physical Review B, 1996. **54**(16): 11169–11186.
4. Perdew J P, K Burke, M Ernzerhof. Generalized gradient approximation made simple. Physical Review Letters, 1996. **77**(18): 3865–3868.